




Coupling the Corrosion-and Pressure-Assisted Stress Buildup Within the Zirconium in PWR Pipes

ASGHAR ARYANFAR^{1,2,4}  ABDEL RAHMAN EL TALLIS,¹
 and JAIME MARIAN³

1.—American University of Beirut, Riad El-Solh, Beirut 1107 2020, Lebanon. 2.—Bahçeşehir University, 4 Çırağan Cd., Beşiktaş, Istanbul 34349, Turkey. 3.—University of California Los Angeles, 400 Westwood Plaza, Los Angeles, CA 90095, USA. 4.—e-mail: aryanfar@caltech.edu

We have developed a new real-time framework for calculating the simultaneous accumulation of oxidation-induced and the internal/external fluid stresses during the corrosion of the zirconium metal, Zr. In order to track such interfacial stress when the zirconium metal turns oxide, we quantify the hypothetical real-time infiltration of the oxygen within the metal matrix in the curved boundary, leading to the augmentation in the volume, and we stoichiometrically compute the resulted equivalent oxide thickness. Subsequently, we calculate the accumulated compressive stress in real-time from both irreversible (plastic) and reversible (elastic) events which could be used for anticipation of the onset of failure. The developed analytical framework could quantify the design parameters for the safe operation of high-pressure pipes in corrosive environments.

List of Symbols

D	Diffusion coefficient ($\text{m}^2 \text{s}^{-1}$)	$\delta r_{\text{PL}}, \delta V_{\text{PL}}$	Vertical (radial) swelling and volume change due to oxidation (m, m^3)
f	Dimensionless stress factor (\square)	δr_{EL}	Vertical (radial) swelling due to Poisson's effect (m)
Ω	Molar volume ($\text{m}^3 \text{mol}^{-1}$)	δr	Total infinitesimal swelling (m)
T	Temperature (K)	δx_{PL}	Horizontal swelling due to oxidation (m)
R_u	Gas constant ($8.3 \text{ J mol}^{-1} \text{ K}^{-1}$)	K	Bulk modulus (Pa)
R_I	Inner radius (m)	$(dt), t$	(Incremental) time (s)
R_O	Outer radius (m)	C	Concentration of oxygen (mol m^{-3})
σ_{EL}	Elastic stress (Pa)	C_0	Concentration of oxygen in water (mol m^{-3})
σ_{PL}	Plastic stress (Pa)	a	Areal coefficient (m^2)
σ_r	Radial stress (Pa)	k	Reaction (corrosion) constant (s^{-1})
σ_θ	Hoop stress (Pa)	N_O	Moles of filled oxygen (\square)
σ_{Tot}	Total stress (Pa)	s	Thickness of oxide scale (m)
P_I	Internal pressure (Pa)	s_c	Critical thickness of oxide scale for failure (m)
P_O	External pressure (Pa)	A_{OX}	Area of oxide (m^2)
r	Radial variable (m)	M	Molar mass (gr mol^{-1})
E	Elastic modulus (Pa)	σ_{uc}	Ultimate compressive strength (Pa)
ν	Poisson's ratio (\square)	k_B	Boltzmann constant (J K^{-1})
$\delta V_M, \delta r_M$	Infinitesimal increase in metallic volume and thickness (m^3, m)	δV_{PL}	Infinitesimal oxide volume (m^3)
$s_{c,I}$	Internal failure thickness (m)	R_{PB}	Pilling-bedworth ratio (\square)
$s_{c,O}$	External failure thickness (m)	dr	Infinitesimal radial variation (m)
u	Infinitesimal radial displacement (m)	$d\theta$	Infinitesimal azimuthal variation (\square)
$(\delta V), V$	(Incremental) volume (m^3)		

(Received June 6, 2022; accepted August 29, 2022)

Published online: 05 October 2022

INTRODUCTION

The oxidation of the metallic pipelines in the cooling section of light water reactors (LWRs) is a crucial factor for the safety assessment and engineering of their material, structural properties,^{1,2} and operational process.³ In particular, zirconium (Zr) has a substantial potential for utilization as a clad to withstand loads under highly oxidative regimes; however, the chemical and mechanical extent that it can resist to the oxidation sets limitations on the reactor's fuel energy extraction rate.⁴⁻⁷

One of the main failure mechanisms in LWR pipes is the stress buildup and the formation of a metal oxide layer, interfacing with the underlying metal.⁸ There are several studies on stress corrosion cracking^{9,10} and failure,^{11,12} rate of crack growth,¹³ and role of grain orientation.¹⁴ In particular, phase-field models have recently been developed for coupling the mechano-chemical effects¹⁵ and dissolution-driven failure.¹⁶

In a corrosion event, the corrosion succeeds the diffusion of oxygen solute from the water into the metal matrix,¹⁷⁻¹⁹ and, since the two stages occur in series, the one causing the lower corrosion rate will be controlling. Typically, the rate of the oxide growth starts the highest in the metal surface and reduces in time, as the oxide thickens and hinders the further diffusion of oxygen in deeper layers, which causes the oxidation interface to breathe harder. However, after a certain achieved oxide thickness, it partially breaks due to compressive stress and chemical degradation, leading to a sudden jump in the oxidation rate, as the oxygen (i.e., water) can penetrate within the cracks in the oxidation surface. This pattern is repeated and forms a series of oxidative reactions, which induces a weakened structure of the overall pipe surface, leading to the susceptibility to total fracture.²⁰⁻²² The kinetics of such reactions have already been explored, with the focus on material composition and chemistry.²³⁻²⁶ The typical increase in the structure's volume is mainly attributed to the Pillar-Bedworth ratio, which translates into the added compressive stresses.²⁷⁻²⁹

Several factors may complicate the corrosion, such as irradiation,³⁰ pressure, temperature,³¹ and chemical kinetics from the side reactions,^{23,32} as well as (sub)-stoichiometric (partial) oxidation³³ and hydration.³⁴

Experimentally, previous studies have explored the corrosion mechanism,³⁵ have used microscopy (optical, SEM, Raman)^{36,37} and visual inspection,³⁸ set up new devices,³⁹ explored the role of environmental sulfide⁴⁰ and other additives, such as fluorine,⁴¹ iodine,⁴² and synthesized composites,^{43,44} used a graphene coating to enhance thermal stability,⁴⁵ and investigated chemical degradation in plastics,⁴⁶ as well as cyclic cooling.⁴⁷

Pressure, among other things, is a driving force for the diffusion of oxygen into the metal, which results in the additional stress buildup.^{27,48,49} This has previously been investigated in both atomic⁵⁰ and continuum⁵¹ scales, where the generated compressive stress weakens the enveloping metal material and expedites the failure.⁵² Having such importance, pressure-dependent research on corrosion lacks sufficiency, particularly in terms of coupling with the corrosion-induced internal stresses.

In this paper, a one-dimensional pressure-induced corrosion kinetics model has been developed in the cylindrical pipelines.⁵³⁻⁵⁶ The diffusion of oxygen from both the concentration gradient⁵⁷ and the external mechanical pressure^{58,59} has been quantified, and the equivalent oxide thickness anticipated. Subsequently, we have developed a framework to compute the resulted effective mechanical compressive stress within the oxidized medium. The developed methodology is useful for designing the range of the parameters for avoiding the failure of PWR cooling pipelines.

METHODOLOGY

Material Properties

The material properties for the framework are expressed in the Table I, and are mainly extracted for Zr with pressurized water. While most of the variables/constants are the typical values from the references, the rest are calculated. For example, the molar volume Ω is calculated via molar mass M and the mass density ρ as:

$$\Omega = \frac{M}{\rho} = \frac{123 \text{ g mol}^{-1}}{5.68 \text{ g cm}^{-3}} \approx 22 \times 10^{-6} \text{ m}^3 \text{ mol}^{-1} \quad (1)$$

As well the oxygen concentration in the water, C_0 is obtained as:

$$C_0 = \frac{\rho}{M} = \frac{1000 \text{ g L}^{-1}}{18 \text{ g mol}^{-1}} = 55 \text{ mol L}^{-1} \quad (2)$$

Framework

During the corrosion event, the infiltration of oxygen within the metal and the subsequent reaction leads to the formation of an oxide layer on the surface of the metal. Figure 1a shows such a formation in our experimental sample. In pipe geometry, this can occur in either the inner or outer boundary of the pipes, as shown in Fig. 1b with distinguishing colors.

During the growth of the thin oxide layer on top of the underneath metallic medium, while the radial boundaries (R_1 , R_0) remain free to move, the lateral (i.e., hoop) boundaries, remain constrained, and the

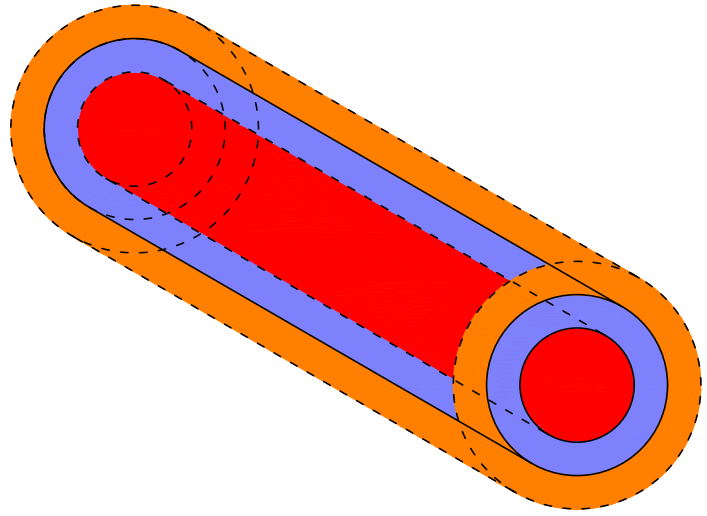
Table I. Model parameters

Variables				Constants			
Par.	Values	Unit	Ref.	Par.	Value	Unit	Ref.
D	1.4×10^{-20} ,	$\text{m}^2 \text{s}^{-1}$	60	k_B	1.38×10^{-23}	J K^{-1}	61
M	123	g mol^{-1}	62	N_A	6.02×10^{23}	atom mol^{-1}	63
R_{PB}	1.56	\square	28,64	R_u	8.314	$\text{J mol}^{-1} \text{K}^{-1}$	63
K	142	GPa	Azom ^a	P_O	15	MPa	65
k	7.1×10^{-6}	s^{-1}	66	P_I	110	MPa	67
f	0.3	\square	51,68	R_O	2.5	mm	69
v	0.34	\square	70	R_I	1.5	mm	69
T	630(357)	K(°C)	33	C_0	55×10^3	mol m^{-3}	Eq. 2
σ_{uc}	1200	MPa	Azom ^{a,b}	dr	4×10^{-4}	m	Assumed
Ω	2.2×10^{-5}	$\text{m}^3 \text{mol}^{-1}$	Eq. 1	dt	1.7×10^{12}	s	Calculated

^a<https://www.azom.com/properties.aspx?ArticleID=133>. ^bFor conservative purposes, the minimum value is considered.



(a) Sample of lab-scale formation of corrosion layers on both internal and external surfaces.



(b) The pipe (blue) with the imposed inner (orange) and outer (red) pressure flows.

Fig. 1. Experimental sample of the corroded pipe (left) and the schematics of the internal/external flows (right) (Color figure online).

misfit stress σ_{EL} builds due to the volumetric difference between the oxide and the metal.

Additionally, in the same direction, the hoop component of the pressure-induced stress σ_θ from the internal/external fluid will be a contributing factor in the same direction. Therefore, the total stress σ_{Tot} will be their sum, as shown in the Eq. 3:

$$\sigma_{Tot} = \sigma_{EL} + \sigma_\theta, \quad (3)$$

and we explain each stress term separately below.

Elastic Stress σ_{EL}

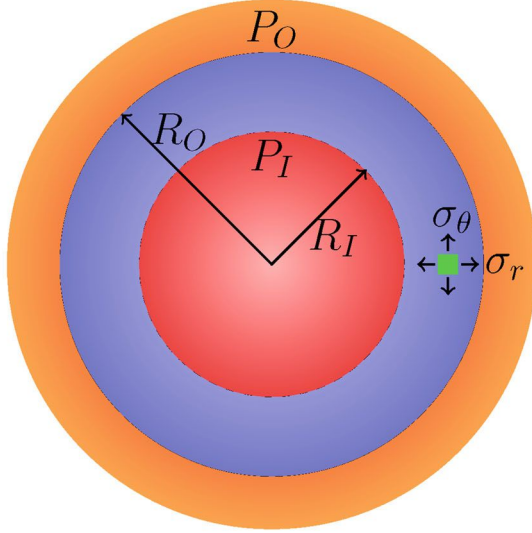
Imposing the internal and external pressures P_I and P_O , the radial σ_r and hoop σ_θ elastic stresses

develop, as shown in Fig. 1b. which are only functions of the radius, r , due to polar symmetry. Cutting out the infinitesimal element shown in Fig. 2b, the balance relationships in the horizontal direction is obtained in Eq. 4 as:⁷¹

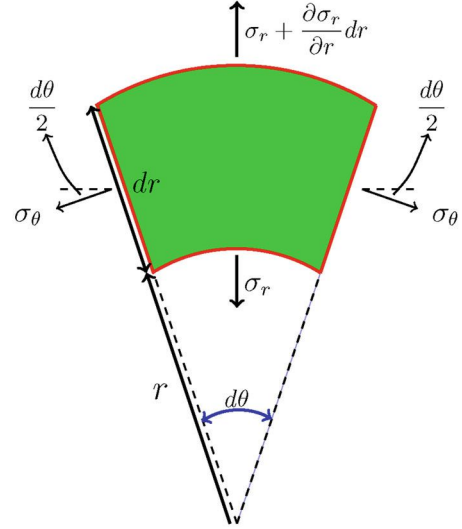
$$\left(\sigma_r + \frac{\partial \sigma_r}{\partial r} dr \right) \cdot (r + dr) d\theta - \sigma_r \cdot r d\theta - 2\sigma_\theta \cdot dr \cdot \frac{d\theta}{2} = 0, \quad (4)$$

where by simplification and ignoring the higher-order terms, we arrive at Lamé's relationship as:⁷²

$$\frac{\partial \sigma_r}{\partial r} + \frac{\sigma_r - \sigma_\theta}{r} = 0 \quad (5)$$



(a) Cross-sectional schematic of the medium with the resulted hoop (σ_θ) and radial (σ_r) stresses



(b) The infinitesimal element analyzed for stress equilibrium.

Fig. 2. Characterization of the stresses and equilibrium forces.

Considering u as the infinitesimal displacement in the radial direction, solving for the radial σ_r and hoop σ_θ stresses, one gets (“Appendix 1”):⁷¹

$$\begin{cases} \sigma_r = \frac{E}{1-\nu^2} \left(\frac{du}{dr} + \nu \frac{u}{r} \right) \\ \sigma_\theta = \frac{E}{1-\nu^2} \left(\frac{u}{r} + \nu \frac{du}{dr} \right) \end{cases} \quad (6)$$

From Fig. 1b, assuming the $\{R_I \text{ and } R_O\}$ are the inner and outer radii of the pipe, respectively, and assigning the boundary conditions for the compressive stresses as $\sigma_r(R_I) = -P_I$ and $\sigma_r(R_O) = -P_O$, the hoop stress σ_θ is finally obtained in Eq. 7 as (“Appendix 1”):

$$\sigma_\theta = \frac{P_I R_I^2 - P_O R_O^2}{R_O^2 - R_I^2} + \left(\frac{R_I^2 R_O^2 (P_O - P_I)}{R_O^2 - R_I^2} \right) \frac{1}{r^2} \quad (7)$$

which is the compressive stress generated by the boundedness in the azimuthal (i.e., hoop) direction.

Corrosion Stress σ_{PL}

Figure 3 illustrates the infinitesimal variation in the volumes by means of the superposition. In the absence of the underneath metallic medium, the oxidation will lead to the free expansion (shown in green). However, due to boundedness from the azimuthal (hoop) direction, the horizontal expansion will translate into additional radial expansion via Poisson’s effect (shown in red). As given in Eq. 8, any swelling in the surface δr , is partially the result of the natural oxidation with plastic irreversible deformation δr_{PL} , as well as the straining due to

elastic lateral compressive stress (the Poisson effect) δr_{EL} , as:

$$\delta r = \delta r_{PL} + \delta r_{EL} \quad (8)$$

The isotropic plastic straining can be explained by Eq. 9 as:

$$\frac{\delta r_{PL}}{r} = \frac{\delta x_{PL}}{x}, \quad (9)$$

where x is the hoop direction. Also, Poisson’s effect is characterized by Eq. 10 as:

$$\frac{\delta r_{EL}}{r} = \nu \frac{\delta x_{PL}}{x} \quad (10)$$

Combining Eqs. 8, 9, and 10, we get the elastic versus the total displacement ratio in Eq. 11 as:

$$\frac{\delta r_{EL}}{r} = \frac{\nu}{1+\nu} \frac{\delta r}{r} \quad (11)$$

On the other hand, considering 2D augmentation (i.e., $\frac{\delta V}{V} \approx \frac{\delta A}{A} \approx \frac{\delta r}{r}$), the infinitesimal growth of the elastic compressive stress $\delta \sigma_{EL}$ will be given in Eq. 12 as:

$$\delta \sigma_{EL} \approx K \frac{\nu}{1+\nu} \frac{dA}{A}, \quad (12)$$

where the fraction $\frac{\nu}{1+\nu}$ is the partial effect of compressive stress on the swelling. The rest of the expansion is due to sole oxidation, which does not generate compressive stress. Therefore, the elastic

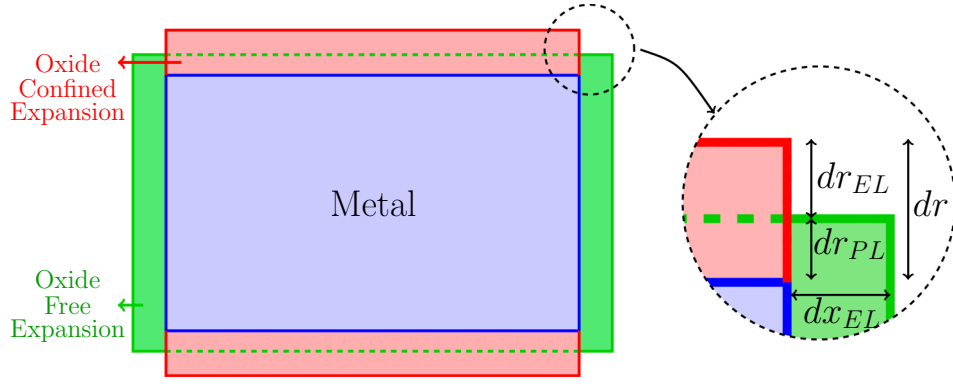


Fig. 3. Swelling due to both oxidation and the lateral compressive stress; blue original metal, green free oxide expansion, red confined oxide expansion (Color figure online).

compressive stress from the corrosion, $\delta\sigma_{EL}$, is caused by the portion of the swelling responsible for Poisson's effect.

During the oxidation, as the oxygen diffuses into the metal matrix, an infinitesimal metallic volume δV_M is removed and then replaced plastically by the respective oxide of higher volume δV_{PL} , such that $\delta V_{PL} = R_{PB}\delta V_M$, and R_{PB}^* is the Pilling-Bedworth ratio,⁷⁴ representing the oxide-to-metal volumetric ratio. Hence, the total augmentation in the surface δr turns into their difference, obtained in Eq. 13 as:

$$\begin{aligned}\delta r &= \delta s - \delta r_M \\ &= \frac{R_{PB} - 1}{R_{PB}} \delta s,\end{aligned}\quad (13)$$

where the fraction $\frac{R_{PB} - 1}{R_{PB}}$ (< 1) shows the partial effect of swelling from the replacement of the metal δV_M with the larger oxide volume δV_{PL} .

Inner Corrosion

The parametrization of the inner corrosion is shown in Fig. 4. The infinitesimal variations in the radial direction δr and the oxide thickness δs are correlated as: $\delta r = -\frac{R_{PB} - 1}{R_{PB}}\delta s$ where the negative sign represents their opposite growth pattern. Hence, integrating from the initial value of $r_0 = R_I$ and $s_0 = 0$ yields Eq. 14 as:

$$r = R_I - \frac{R_{PB} - 1}{R_{PB}} s \quad (14)$$

and, additionally, the infinitesimal oxide area change dA in the radius r is given in Eq. 15 as:

$$dA = 2\pi \left(R_I - \frac{R_{PB} - 1}{R_{PB}} s \right) \frac{R_{PB} - 1}{R_{PB}} ds \quad (15)$$

Furthermore, the total oxidized area A is given by Eq. 16:

$$A = \pi \left(R_O^2 - \left(R_I - \frac{R_{PB} - 1}{R_{PB}} s \right)^2 \right) \quad (16)$$

Hence, combining Eqs. 12, 13, 15, and 16, we achieve the elastic stress σ_{EL} given in Eq. 17 as ("Appendix 2"):

$$\begin{aligned}\sigma_{EL} &= K \frac{\nu}{1 + \nu} \ln \left(1 + \frac{R_{PB} - 1}{R_{PB}} \left(\frac{2R_I}{R_O^2 - R_I^2} \right) s \right. \\ &\quad \left. + \left(\frac{R_{PB} - 1}{R_{PB}} \right)^2 \frac{s^2}{R_O^2 - R_I^2} \right)\end{aligned}\quad (17)$$

Outer Corrosion

During the outer corrosion, which is parametrized in Fig. 4, the correlation would be $\delta r = \frac{R_{PB} - 1}{R_{PB}}\delta s$, and δs and δr are in the same direction. Integrating from the initial values of $r_0 = R_O$ and $s_0 = 0$ we get Eq. 18:

$$r = R_O + \frac{R_{PB} - 1}{R_{PB}} s \quad (18)$$

Respectively, the infinitesimal oxide area change dA is attained in Eq. 19 as:

$$dA = 2\pi \left(R_O + \frac{R_{PB} - 1}{R_{PB}} s \right) \frac{R_{PB} - 1}{R_{PB}} ds \quad (19)$$

and the total oxidized area is given in Eq. 20 as:

$$A = \pi \left(\left(R_O + \frac{R_{PB} - 1}{R_{PB}} s \right)^2 - R_I^2 \right) \quad (20)$$

Therefore, combining Eqs. 12, 13, 19, and 20, we get the elastic stress σ_{EL} obtained in Eq. 21 as ("Appendix 3"):

*For Zr, $R_{PB} = 1.56$.⁷³

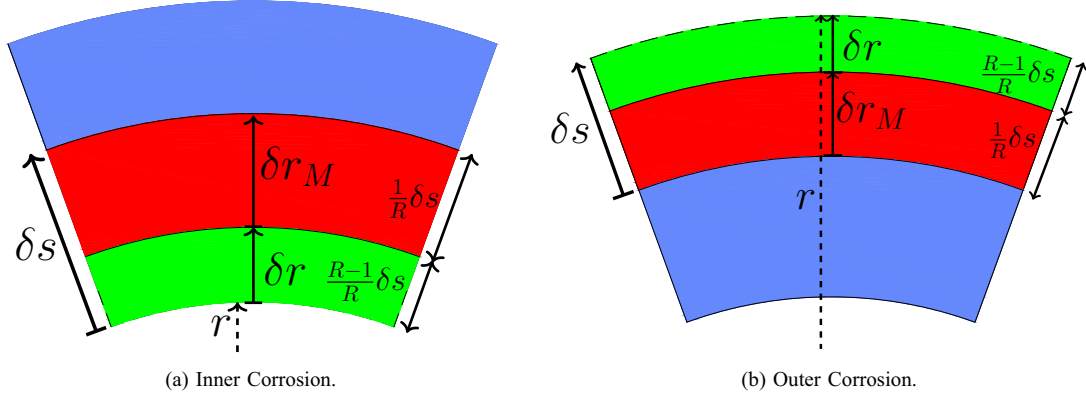


Fig. 4. Schematics of the inner (a) and outer (b) corrosion; blue metal layer, red oxide layer, green augmented volume due to oxidation (Color figure online).

$$\sigma_{EL} = K \frac{v}{1+v} \ln \left(1 + \frac{R_{PB} - 1}{R_{PB}} \left(\frac{2R_O}{R_O^2 - R_I^2} \right) s + \left(\frac{R_{PB} - 1}{R_{PB}} \right)^2 \frac{s^2}{R_O^2 - R_I^2} \right) \quad (21)$$

Corrosion Kinetics

The corrosion consists of the two simultaneous events of diffusion and reaction, which establishes a mass-balance relationship. While the diffusion event carries the oxygen atoms inside the metal, the reaction term consumes them to turn metal into the oxide. For simplicity, here we perform superposition for the diffusion-reaction event and explore each of them individually below.

I: Oxygen Infiltration (Diffusion)

Regarding the change in the concentration due to sole diffusion $\left(\frac{dC}{dt} \right)_{\text{Diff}}$, the rate of influx is controlled by the gradient of the oxygen concentration C and stress σ as:^{51,57}

$$\left(\frac{dC}{dt} \right)_{\text{Diff}} = -D \nabla \cdot \left(\nabla C + \frac{f\Omega}{R_u T} C \nabla \sigma \right) \quad (22)$$

where D is the diffusion coefficient, f is the dimension-less contraction factor⁶⁸ ($0 < f < 1$), Ω is the molar volume, R_u is the universal gas constant, and T is the temperature. Such a relationship in the radial distance for the concentration $C(r, t)$ can be expressed as (“Appendix 4”):

Table II. The boundary conditions for inner or outer corrosion

Inner corrosion (P_I)	Outer corrosion (P_O)
$\begin{cases} C(R_I, t) = C_0 \\ \frac{\partial C(R_O, t)}{\partial r} = 0 \end{cases}$	$\begin{cases} \frac{\partial C(R_I, t)}{\partial r} = 0 \\ C(R_O, t) = C_0 \end{cases}$

$$\left(\frac{dC}{dt} \right)_{\text{Diff}} = D \frac{\partial^2 C}{\partial r^2} + \alpha(r) \frac{\partial C}{\partial r} + \beta(r) C \quad (23)$$

where $R_I < r < R_O$ and the range of time are considered as $0 < t < \sim \frac{R_O^2}{D}$. The coefficients of $\alpha(r)$ and $\beta(r)$ are obtained as (“Appendix 1”):

$$\begin{cases} \alpha(r) = -\frac{2Df\Omega B}{R_u T r^3} \\ \beta(r) = 6 \frac{f\Omega B}{R_u T r^4} \end{cases} \quad (24)$$

and the derivation is provided in the Appendix. The corresponding initial condition would be the intact metal (i.e., no oxygen) as:

$$C(r, 0) = 0 \quad (25)$$

The respective boundary conditions for both inner and outer corrosion are shown in Table II, where the constant boundary condition shows the contact with the ambient oxygen supply, whereas the zero derivative condition represents no escape of the oxygen from the respective interface.

Numerical Solution

The non-linear Eq. 23 can be numerically solved by segmenting the time and space intervals, δt and δr , respectively. If C_I^j represents the time t^j and the radial distance r_I , respectively, we utilize the forward move in the time and space and re-write Eq. 23 as:

$$\frac{C_I^{j+1} - C_I^j}{\delta t} = D \frac{C_{I+1}^j + C_{I-1}^j - 2C_I^j}{\delta r^2} + \alpha(r) \frac{C_{I+1}^j - C_I^j}{\delta r} + \beta(r) C_I^j \quad (26)$$

re-arranging the concentration values in the time giving the neighbor-dependent concentration relationship in Eq. 27 as:

$$C_I^{j+1} = Q_1 C_I^j + Q_2 C_{I+1}^j + Q_3 C_{I-1}^j \quad (27)$$

and the Q_I s are the quotients extracted as in Eq. 28:

$$\begin{cases} Q_1 = 1 - \frac{2D\delta t}{\delta r^2} + \frac{\alpha(r)\delta t}{\delta r} + \beta(r)\delta t \\ Q_2 = \frac{\alpha(r)\delta t}{\delta r} \\ Q_3 = \frac{D\delta t}{\delta r^2} \end{cases} \quad (28)$$

Table III. The boundary conditions for the numerical solution

Inner corrosion (P_I)	Outer corrosion (P_O)
$\begin{cases} C_1^j = C_0 \\ C_{end-1}^j = C_{end}^j \end{cases}$	$\begin{cases} C_1^j = C_2^j \\ C_{end}^j = C_0 \end{cases}$

Also, the boundary conditions in Table II are translated into Table III.

Hence, the resolution criterion is obtained conservatively as ("Appendix 5"):

$$\delta t < \left(\frac{2D}{\delta r^2} + \frac{2fD\Omega B}{R_u Tr^3 \delta r} - \frac{6fD\Omega B}{R_u Tr^4} \right)^{-1} \quad (29)$$

In order enlarge the application to the broader ranges of scales, the dimensionless parameters are defined by normalizing as:

$$\hat{r} = \frac{r - R_I}{R_O - R_I}, \hat{C} = \frac{C}{C_0}, \hat{t} = \frac{D}{R_O^2} t, \hat{s} = \frac{s}{R_O - R_I} \quad (30)$$

since $R_I \leq r \leq R_O$ and $C \leq C_0$, hence $0 \leq \hat{C}, \hat{r}, \hat{s} \leq 1$. The evolution of the concentration profile based on the parameters given in Table I for inner or outer corrosion is shown in Fig. 5a and b, respectively.

II: Oxygen Consumption

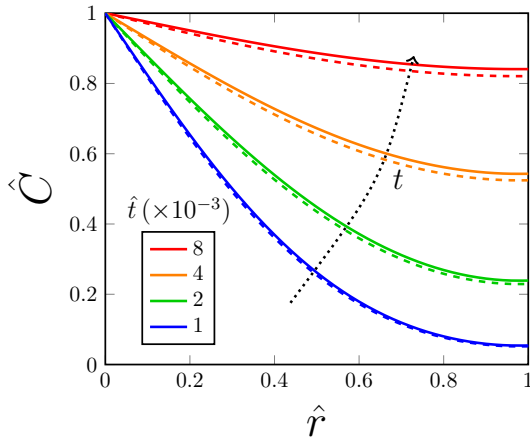
The infiltrated oxygen becomes simultaneously consumed via a corrosion reaction with the rate of $\left(\frac{dC}{dt}\right)_{\text{Rxn}}$, which is obtained from:⁷³

$$\left(\frac{dC}{dt}\right)_{\text{Rxn}} = -kC, \quad (31)$$

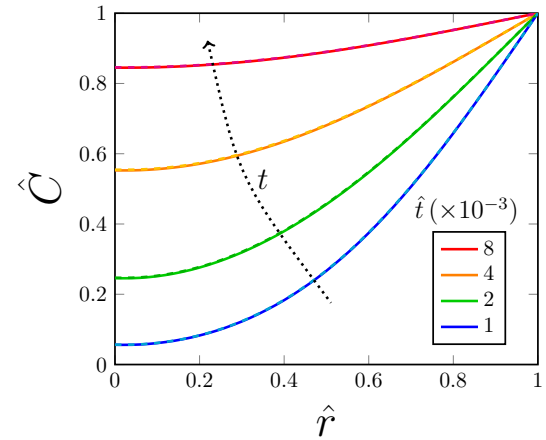
where k is the reaction constant for the oxidation.

Comparing the rates of the diffusion $\left(\frac{dC}{dt}\right)_{\text{Diff}}$ and

reaction $\left(\frac{dC}{dt}\right)_{\text{Rxn}}$ from the realistic values given in Table I, we get:



(a) Inner Corrosion.



(b) Outer Corrosion.

Fig. 5. The evolution of *hypothetical* oxygen concentration during the inner (left) and outer (right) corrosion; dashed lines represent the no-pressure case scenario.

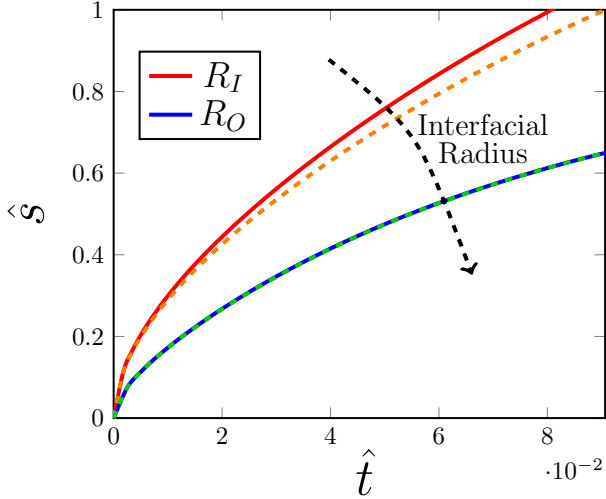


Fig. 6. Evolution of the oxide thickness \hat{s} in the locations of the inner R_I and outer R_O radii; solid with pressure, dashed no pressure.

$$\begin{cases} \left(\frac{dC}{dt}\right)_{\text{Diff}} \sim D \frac{C_0}{R_0} \sim 10^{-15} \text{ mol s}^{-1} \\ \left(\frac{dC}{dt}\right)_{\text{Rxn}} \sim k C_0 \sim 10^{-1} \text{ mol s}^{-1} \end{cases} \quad (32)$$

which means that the rate of consumption is far larger than the diffusion,³³ albeit the events are simultaneous. Therefore, upon reaching the reaction sites, the earliest event to occur is the reaction and the entire oxygen is consumed to stoichiometric saturation. In fact, the hypothetical concentration profiles shown in Fig. 5a and b never become established physically in the presence of exceptionally large reaction rates, and the thickness of the oxide scale, s , will be their reaction-equivalent case scenario. Hence, for corrosion in the vicinity of the radial distance, r , we get Eq. 33 by means of mass balance:

$$s = \frac{\Omega}{2\pi r} \int_{R_I}^{R_O} C dA, \quad (33)$$

where Ω is the molar volume of the oxygen, $2\pi r$ is the peripheral area of the oxidation interface in the radial distance r , C is the hypothetically established concentration throughout the radial range $R_I < r < R_O$, and dA is the respective infinitesimal area. Figure 6 illustrates the evolution of the oxide thickness \hat{s} versus time \hat{t} in dimensionless form for both inner or outer corrosion, where the role of the location on the rate of corrosion has been emphasized.

RESULTS AND DISCUSSION

From Fig. 5, it can be seen that the filling of the oxygen concentration within the medium has a higher rate for the pressurized case. The underlying

reason is the radial stress σ_r , which directly enforces a higher flux of the oxygen than of typical diffusion.

The accumulated stresses in the inner and outer corrosion based on Eqs. 17 and 21 are presented within Fig. 7, and have been compared with the experimental data, which are in larger part in close proximity to each other. The relative earlier failure of the prior could be attributed to the difference in their experimental setup and process.^{75,76} For instance, Garzarolli et al.⁷⁷ has performed prior irradiation to the samples as well as using a boiling water reactor (low pressure) condition, which makes a deeper (i.e., weaker) nodular oxide [vs. the uniform oxidation in a pressurized water reactor (PWR; high pressure)] and could fail earlier. Also, Stehle et al.⁷⁸ have considered the hydride role and orientation, which additionally contributes to the failure. However, the results of Hillner et al.,⁶⁹ which refer the PWR conditions, are in closer agreement with our results.

The linear appearance in these graphs shows that the fracture of the material occurs upon the formation of a thin layer, where $s \ll R_O - R_I$. In fact, one can approximate the corrosion stress σ_{EL} via the Taylor expansion, ignoring the higher-order terms[†]. Therefore, linearization of Eqs. 17 and 21 yields the accumulated elastic stress at the given interfacial radius, r , as:

$$\sigma_{EL} \approx K \frac{\nu}{1+\nu} \frac{R_{PB}-1}{R_{PB}} \frac{2rs}{R_O^2 - R_I^2} \quad (34)$$

which means that the amount of the accumulated stress σ_{EL} is proportional to the radius of the corrosion, r . Looking more closely to the non-linear form of the stress in Eqs. 17 and 21, it is initially obvious that $\frac{\partial \sigma_{EL}}{\partial s} > 0$. Additionally, we realize that:

$$\frac{d^2 \sigma_{EL}}{ds^2} \approx - \left(\frac{R_{PB}-1}{R_{PB}} \right)^2 \left(\frac{2R_I}{R_O^2 - R_I^2} \right)^2 < 0 \quad (35)$$

and, therefore, the form of the stress accumulation versus oxide thickness is concave, which becomes more apparent during extended corrosion scale. Also, for the corrosion in the vicinity of a given radial distance, r , the critical thickness s_c , where the medium fails due to compressive stress, is obtained from setting $\sigma_{EL} = \sigma_{u,c}$ in Eq. 34 as:

$$s_c = \frac{\sigma_{u,c}}{K} \frac{1+\nu}{\nu} \frac{R_{PB}}{R_{PB}-1} \frac{R_O^2 - R_I^2}{2r}, \quad (36)$$

where $\sigma_{u,c}$ is the compressive strength of the material. Furthermore, the interpretation from Eq. 36 yields:

$$r \uparrow \Rightarrow s_c \downarrow \quad (37)$$

[†]In when x is small.

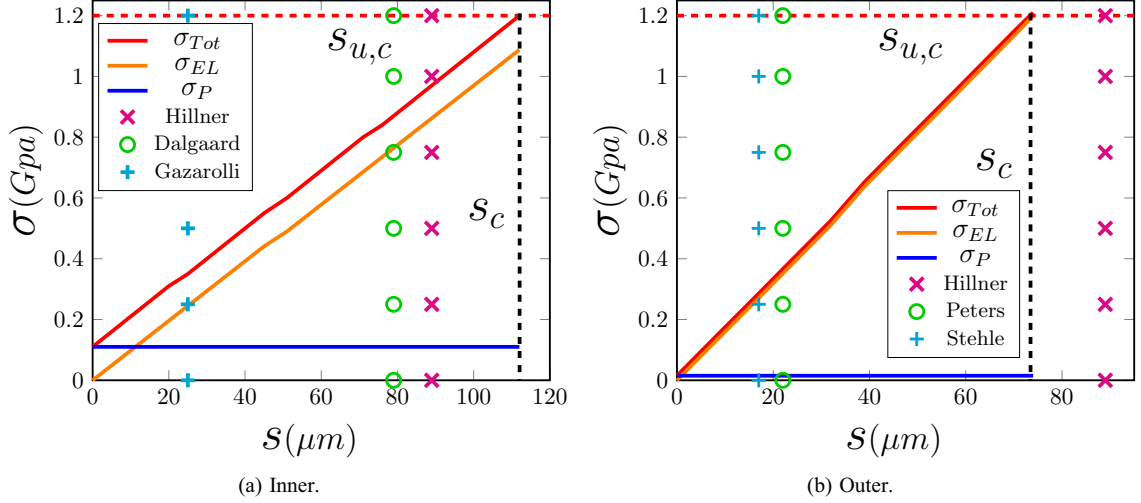


Fig. 7. The stress buildup versus the thickness, illustrating the total accumulated stress at the verge of failure. The range of previous experimental findings is illustrated via the blue region (Color figure online).

which implies that the inner corrosion has a faster rate of growth, since less material is needed to generate a similar oxide thickness, s , as shown in Fig. 6 (i.e., since $R_O > R_I$, therefore $s_{c,O} < s_{c,I}$). Thus, having a similar oxide thickness, s , the amount of the accumulated stress for the outer corrosion is larger than for the inner corrosion, which is reasonable, since the outer boundary possesses a higher amount of the material leading to the compressive stress compared with the inner. The main reason for the decrease in the rate of oxide growth has been attributed to the lower accessibility of the inner regions of the corrosion to the supply of oxygen in the boundary,⁷³ where the larger the depth of the oxide, the harder the corrosion interface can breathe.

Regarding the variation of the critical thickness s_c versus the Poisson ratio, from Eq. 36 we get:

$$\frac{\partial s_c}{\partial \nu} \sim -\frac{1}{\nu^2} < 0, \quad (38)$$

which means their inverse correlation. In fact, it is obvious that the more the lateral effect imposed by the Poisson ratio, the earlier the medium breaks.

Finally, regarding the resolution criterion provided in Eq. 29, the extra terms show the need for a finer segmentation in time δt versus the radial segmentation δr in the polar-to-planar diffusion where solely $\delta t \leq \frac{\delta r^2}{2D}$.⁷⁹ This can be attributed to the extra term in the gradient in the polar coordinates relative to the planar coordinate, which requires a more strict criterion for time versus space discretization.

CONCLUSION

We have developed a time and thickness-dependent framework for the buildup of the compressive stresses within the oxide medium, via considering the fractional role of the swelling on generating the stress. Also, we have coupled the resulting stress with the pressure-induced fluid pressure for either the inner or outer corrosion. Performing the superposition for the accumulation and consumption of the oxygen, we compute the diffused oxygen into the metal and obtain the resulting equivalent oxide thickness stoichiometrically, which represents the fractional swelling of the surface via metal removal and oxide addition. Adding the elastic stress due to pressure as well as the corrosion effect, we use it as a measure for anticipating the onset of mechanical failure. Our formulation, which is based on the physical parameters involved, could be useful for the design and maintenance process of high-pressure pipes in aqueous environments.

ACKNOWLEDGEMENTS

The authors would like to thank the support from Masri Institute at American University of Beirut, Grant Award No. 103919 for the student Abdel Rahman El Tallis.

DATA AVAILABILITY

The raw data for producing the results in this manuscript are freely available upon request from the corresponding author at aryanfar@caltech.edu.

CONFLICT OF INTEREST

The authors declare that they have no competing financial interests to influence the work reported in this paper.

APPENDIX

Here, we present the detailed steps for establishing the relationships shown in the article.

1. Elastic Stress σ_{EL} (Eq. 7)

Imposing the internal and external pressures P_I and P_O , the radial σ_r and hoop σ_θ elastic stresses develop, as shown in Fig. 1b which are the only function of radius r due to polar symmetry. Cutting out the infinitesimal element shown in Fig. 2b, the balance relationships in the horizontal direction would be:

$$\sum F_x = 0$$

therefore:

$$\left(\sigma_r + \frac{\partial \sigma_r}{\partial r} dr \right) \cdot (r + dr) d\theta - \sigma_r \cdot r d\theta - 2\sigma_\theta \cdot dr \cdot \frac{d\theta}{2} = 0$$

where by simplification and ignoring the higher-order terms, we arrive at Lamé's relationship as:^{71,72}

$$\frac{\partial \sigma_r}{\partial r} + \frac{\sigma_r - \sigma_\theta}{r} = 0$$

Regarding the strain ϵ , if u is the infinitesimal displacement in the radial direction, from the Hook's generalized law, one gets:⁷¹

$$\begin{cases} \epsilon_r = \frac{du}{dr} = \frac{1}{E}(\sigma_r - \nu\sigma_\theta) \\ \epsilon_\theta = \frac{u}{r} = \frac{1}{E}(\sigma_\theta - \nu\sigma_r) \end{cases}$$

Solving for the radial σ_r and hoop σ_θ stresses and replacing in terms of the infinitesimal displacement, u , one gets:

$$\begin{cases} \sigma_r = \frac{E}{1-\nu^2} \left(\frac{du}{dr} + \frac{u}{r} \right) \\ \sigma_\theta = \frac{E}{1-\nu^2} \left(\frac{u}{r} + \nu \frac{du}{dr} \right) \end{cases} \quad (39)$$

replacing the Eq. 39 into the compatibility Eq. 5 and simplifying we get:

$$\frac{d}{dr} \left(\frac{1}{r} \frac{d}{dr} (u \cdot r) \right) = 0$$

where integrating leads to:

$$u = C_1 r + \frac{C_2}{r}$$

From Fig. 1b, assuming the $\{R_I, R_O\}$ are inner and outer radii of the pipe, respectively, and assigning the boundary conditions for the compressive stresses as $\sigma_r(R_I) = -P_I$ and $\sigma_r(R_O) = -P_O$, the hoop stress σ_P is finally obtained as:

$$\begin{cases} \sigma_r = A + \frac{B}{r^2} \\ \sigma_\theta = A - \frac{B}{r^2} \end{cases} \quad (40)$$

where A and B are constants obtained by the following relationships:

$$\begin{cases} A = \frac{P_I R_I^2 - P_O R_O^2}{R_O^2 - R_I^2} \\ B = \frac{R_I^2 R_O^2 (P_O - P_I)}{R_O^2 - R_I^2} \end{cases} \quad (41)$$

Since the compressive stress causing the failure is the hoop direction, therefore $\sigma_P = \sigma_\theta$, and hence Eq. 7 is obtained as:

$$\sigma_P = \frac{P_I R_I^2 - P_O R_O^2}{R_O^2 - R_I^2} + \left(\frac{R_I^2 R_O^2 (P_O - P_I)}{R_O^2 - R_I^2} \right) \frac{1}{r^2} \quad (42)$$

which is the compressive stress generated by the boundedness in the azimuthal (i.e., hoop) direction.

2. Corrosion Stress (Eq. 17)

$$\begin{aligned} \sigma_{EL} &= K \frac{\nu}{1+\nu} \frac{dA}{A} \\ &= K \frac{\nu}{1+\nu} \int_0^s \frac{2\pi \left(R_I - \frac{R-1}{R} s \right) \frac{R-1}{R} ds}{\pi \left(R_O^2 - \left(R_I - \frac{R_{PB}-1}{R_{PB}} s \right)^2 \right)} \\ &= K \frac{\nu}{1+\nu} \int_0^s \left(\frac{\frac{R-1}{R}}{R_O + R_I - \frac{R_{PB}-1}{R_{PB}} s} + \frac{\frac{R-1}{R}}{R_O - R_I + \frac{R_{PB}-1}{R_{PB}} s} \right) ds \\ &= K \frac{\nu}{1+\nu} \left(\ln \left(R_O + R_I - \frac{R-1}{R} s \right) \Big|_0^s + \ln \left(R_O - R_I + \frac{R-1}{R} s \right) \Big|_0^s \right) \\ &= K \frac{\nu}{1+\nu} \left(\ln \left(1 - \frac{R-1}{R} \frac{s}{R_O + R_I} \right) + \ln \left(1 + \frac{R-1}{R} \frac{s}{R_O - R_I} \right) \right) \\ &= K \frac{\nu}{1+\nu} \left(\ln \left(1 + \frac{R-1}{R} \frac{s}{R_O - R_I} - \frac{R-1}{R} \frac{s}{R_O + R_I} + \left(\frac{R-1}{R} \right)^2 \frac{s^2}{R_O^2 - R_I^2} \right) \right) \\ &= K \frac{\nu}{1+\nu} \ln \left(1 + \frac{R-1}{R} \left(\frac{2R_I}{R_O^2 - R_I^2} \right) s + \left(\frac{R-1}{R} \right)^2 \frac{s^2}{R_O^2 - R_I^2} \right) \end{aligned}$$

3. Corrosion Stress (Eq. 21)

$$\begin{aligned}\sigma_{EL} &= K \frac{v}{1+v} \int_0^s \frac{2\pi \left(R_0 + \frac{R-1}{R}s\right) \frac{R-1}{R} ds}{\pi \left(\left(R_0 + \frac{R-1}{R}s\right)^2 - R_1^2 \right)} \\ &= K \frac{v}{1+v} \int_0^s \left(\frac{\frac{R-1}{R}}{R_0 + \frac{R-1}{R}s - R_1} + \frac{\frac{R-1}{R}}{R_0 + \frac{R-1}{R}s + R_1} \right) ds \\ &= K \frac{v}{1+v} \left(\ln \left(1 + \frac{R-1}{R} \frac{s}{R_0 - R_1} \right) + \ln \left(1 + \frac{R-1}{R} \frac{s}{R_0 + R_1} \right) \right) \\ &= K \frac{v}{1+v} \ln \left(1 + \frac{R-1}{R} \left(\frac{2R_0}{R_0^2 - R_1^2} \right) s + \left(\frac{R-1}{R} \right)^2 \frac{s^2}{R_0^2 - R_1^2} \right)\end{aligned}$$

4. Equation 23

Translating Eq. 22 into a 1D radial direction, we get:

$$\begin{aligned}\left(\frac{dC}{dt} \right)_{\text{Diff}} &= D \nabla \cdot \left(\nabla C + \frac{f\Omega}{R_u T} C \nabla \sigma_r \right) \\ &= D \frac{\partial}{\partial r} \left(\frac{\partial C}{\partial r} + \frac{f\Omega}{R_u T} C \frac{\partial \sigma_r}{\partial r} \right)\end{aligned}$$

The σ_r is obtained from Eqs. 40 and 41, therefore:

$$\frac{\partial \sigma_r}{\partial r} = -\frac{2B}{r^3}, \text{ replacing gives:}$$

$$\begin{aligned}\left(\frac{dC}{dt} \right)_{\text{Diff}} &= D \frac{\partial}{\partial r} \left(\frac{\partial C}{\partial r} - \frac{2f\Omega CB}{R_u T r^3} \right) \\ &= D \left(\frac{\partial^2 C}{\partial r^2} - \frac{2f\Omega B}{R_u T r^3} \frac{\partial C}{\partial r} + 6 \frac{f\Omega B}{R_u T r^4} C \right) \\ &= D \frac{\partial^2 C}{\partial r^2} + \alpha(r) \frac{\partial C}{\partial r} + \beta(r) C\end{aligned}$$

and the coefficients α and β are obtained, respectively, as:

$$\alpha(r) = -\frac{2Df\Omega B}{R_u T r^3}, \beta = 6 \frac{fD\Omega B}{R_u T r^4}$$

5. Equation 29

In order to have a stable solution, we need to have $Q_1 > 0$, hence:

$$1 - \frac{2D\delta t}{\delta r^2} + \frac{\alpha(r)\delta t}{\delta r} + \beta(r)\delta t > 0$$

replacing the α and β values gives:

$$1 - \frac{2D\delta t}{\delta r^2} - \frac{2Df\Omega B}{R_u T r^3} \frac{\delta t}{\delta r} + \frac{6fD\Omega B}{R_u T r^4} \delta t > 0$$

which means that:

$$\delta t < \left(\frac{2D}{\delta r^2} + \frac{2fD\Omega B}{R_u T r^3 \delta r} - \frac{6fD\Omega B}{R_u T r^4} \right)^{-1} \checkmark$$

REFERENCES

1. A. Neil North and D. MacLeod. Corrosion of metals, in *Conservation of Marine Archaeological Objects* (Elsevier, 1987), pp. 68–98.
2. H.H. Strehblow and P. Marcus. Fundamentals of corrosion, *Corrosion Mechanisms in Theory and Practice*, pp. 1–104 (2012).
3. D.R. Knittel and A. Bronson, *Corrosion* 40(1), 9 (1984).
4. P. Bossis, D. Pecheur, K. Hanifi, J. Thomazet, and M. Blat, Comparison of the high burn-up corrosion on m5 and low tin zircaloy-4, in *Zirconium in the Nuclear Industry: 14th International Symposium*. ASTM STP 1467, 494 (2006).
5. A.S. Zaimovskii, *Soviet Atom. Energy* 45(6), 1165 (1978).
6. R.A. Causey, D.F. Cowgill, and R.H. Nilson, *Review of the Oxidation Rate of Zirconium Alloys Report* (Sandia National Laboratories, 2005).
7. E. Hillner, *Zirconium Nucl. Ind.* 633, 211 (1977).
8. A.T. Motta, A. Yilmazbayhan, J. Marcelo, G. da Silva, R.J. Comstock, G.S. Was, J.T. Busby, E. Gartner, Q. Peng, Y.H. Jeong, and J.Y. Park, *J. Nucl. Mater.* 371(1), 61 (2007).
9. A.A. Kharkov, A.A. Alkhimenko, N.O. Shaposhnikov, and E.L. Alekseeva, *Mater. Phys. Mech.* 47(3), (2021).
10. A. Contreras, M. Salazar, A. Albiter, R. Galván, and O. Vega, *Assessment of stress corrosion cracking on pipeline steels weldments used in the petroleum industry by slow strain rate tests* (Arc Welding, IntechOpen Zagreb, Croatia, 2011), p. 144.
11. A.H. Akhi and A.S. Dhar, *Eng. Fract. Mech.* 250, 107778 (2021).
12. Y. Qin, V. Litvinov, W. Chassé, J. Sun, and Y. Men, *Polymer* 252, 124938 (2022).
13. I.V. Ryakhovskikh and R.I. Bogdanov, *Eng. Fail. Anal.* 121, 105134 (2021).
14. Z. Wang, P. Wang, D. Zeng, T. Shi, and W. Deng, *Materials* 15(3), 801 (2022).
15. C. Lin and H. Ruan, *Electrochimica Acta* 395, 139196 (2021).
16. C. Cui, R. Ma, and E. Martínez-Pañeda, *J. Mech. Phys. Solids* 147, 104254 (2021).
17. B. Cox, *J. Nucl. Mater.* 336(2), 331 (2005).
18. B. Cox, *J. Nucl. Mater.* 170(1), 1 (1990).
19. A.T. Motta, A. Couet, and R.J. Comstock, *Annu. Rev. Mater. Res.* 45, 311 (2015).
20. D.J. Young, *High Temperature Oxidation and Corrosion of Metals*, vol. 1 (Elsevier, Berlin, 2008).
21. T. El Maaddawy and K. Soudki, *Cem. Concrete Compos.* 29(3), 168 (2007).
22. T.R. Allen, R.J.M. Konings, and A.T. Motta, *Compreh. Nucl. Mater.* 5, 49 (2012).
23. P. Jacques, F. Lefebvre, and C. Lemaignan, *J. Nuclear Mater.* 264(3), 239 (1999).
24. S. Kass, *J. Nucl. Mater.* 29(3), 315 (1969).
25. C.M. Eucken, P.T. Finden, S. Trapp-Pritsching, and H.G. Weidinger, Influence of chemical composition on uniform corrosion of zirconium-base alloys in autoclave tests. in *Zirconium in the Nuclear Industry Eighth International Symposium*, (ASTM International, 1989) 3.
26. G.S. Frankel, *Fundamentals of Corrosion Kinetics* (Springer, 2016), pp.17–32.
27. P. Jacques, F. Lefebvre, and C. Lemaignan, *J. Nucl. Mater.* 264(3), 249 (1999).
28. K. Forsberg, M. Limback, and A.R. Massih, *Nucl. Eng. Des.* 154(2), 157 (1995).
29. B. Lustman and F. Kerze, *The Metallurgy of Zirconium*, vol. 4 (McGraw-Hill Book Company, 1955).
30. E. Alat, J. Hu, D. Wolfe, and A. Motta. Corrosion and ion irradiation behavior of ceramic-coated nuclear fuel cladding, in *Zirconium in the Nuclear Industry: 19th International Symposium* (ASTM International, 2021), pp. 149–171.
31. N. Lin, Q. Liu, J. Zou, D. Li, S. Yuan, Z. Wang, and B. Tang, *RSC Adv.* 7(22), 13517 (2017).

32. G.P. Sabol and G.D. Moan, in *Zirconium in the Nuclear Industry: Twelfth International Symposium* (ASTM International, 2000), vol. 1354.
33. M. Reyes, A. Aryanfar, S.W. Baek, and J. Marian, *J. Nucl. Mater.* 509, 550 (2018).
34. A.T. Motta, L. Capolungo, L.-Q. Chen, M.N. Cinbiz, M.R. Daymond, and D.A. Koss, *J. Nucl. Mater.* 518, 440 (2019).
35. M. Preuss, A review of early findings within the collaborative research programme muzic: Mechanistic understanding of zirconium corrosion, in *Zirconium in the Nuclear Industry: 19th International Symposium* (ASTM International, 2021).
36. J. Li, M. Elboujdaini, B. Fang, R.W. Revie, and M.W. Phaneuf, *Corrosion* 62(4), 316 (2006).
37. M. Mermoux and C. Duriez, *J. Raman Spectrosc.* 52(12), 2131 (2021).
38. A.R. Khasanova, *J. Phys. Conf. Ser.* **2176**, 012051 (2022).
39. K. Wilczynska, M. Bono, D. Le Boulch, M. Fregonese, V. Chabretou, N. Mozzani, and L. Barbie, Development and validation of a new experimental device for studies of iodine stress corrosion cracking of zirconium alloys, in *19th International Conference on Environmental Degradation of Materials in Nuclear Power Systems-Water Reactors* (2019).
40. M. Kimura, N. Totsuka, T. Kurisu, K. Amano, J. Matsuyama, and Y. Nakai, *Corrosion* 45(4), 340 (1989).
41. B. Gwinner, F. Balbaud-Célrier, P. Fauvet, N. Gruet, P. Laghoutaris, F. Miserque, and R. Robin, *Corros. Sci.* 201, 110284 (2022).
42. Y. Li, C. Ge, Y. Liu, G. Li, X. Dong, G. Zongxing, and Y. Zhang, *Int. J. Min. Metall. Mater.* 29(4), 586 (2022).
43. X.-F. Ma, Y.-W. Wu, J. Tan, C.-Y. Meng, L. Yang, W.-A. Dang, and X.-J. He, *Surf. Coat. Technol.* 358, 521 (2019).
44. Q.S. Chen, C.H. Liu, J.P. Long, J. Wang, R.Q. Zhang, H.Y. Yang, W. Zhang, F.Y. Yao, S. Zhao, and Q. Zhang, *Mater. Res. Exp.* 6(8), 086511 (2019).
45. X. Sun, F. Gong, M. Hao, W. Lei, C. Yin, Z. Sun, and R. Xiao, *Appl. Surf. Sci.* 582, 152484 (2022).
46. B.-H. Choi, A. Chudnovsky, and K. Sehanobish, *Int. J. Fract.* 145(1), 81 (2007).
47. S. Mohanty, S. Majumdar, and K. Natesan, *A Review of Stress Corrosion Cracking/Fatigue Modeling for Light Water Reactor Cooling System Components* (Nuclear Engineering Division Argonne National Laboratory, Argonne, IL, 2012).
48. X. Guo, L. Junqiang, P. Lai, Z. Shen, W. Zhuang, Z. Han, L. Zhang, and S. Lozano-Perez, *Corros. Sci.* 202, 110300 (2022).
49. C. Tang, M. Große, S. Ulrich, M. Klimenkov, and U.H. Jürgen, *Surf. Coat. Technol.* 419, 127263 (2021).
50. H. Mehrer, Diffusion in solids under pressure, in *Defect and Diffusion Forum* (Trans Tech Publ, 2011), vol. 309, pp. 91–112.
51. F.-Z. Xuan, S.-S. Shao, Z. Wang, and S.-T. Tu, *J. Phys. D Appl. Phys.* 42(1), 015401 (2008).
52. R.L. De Orío, H. Ceric, and S. Selberherr, *Microelectron. Reliab.* 50(6), 775 (2010).
53. M. Ahammed and R.E. Melchers, *Int. J. Press. Vessels Pip.* 69(3), 267 (1996).
54. S.-X. Li, S.-R. Yu, H.-L. Zeng, J.-H. Li, and R. Liang, *J. Pet. Sci. Eng.* 65(3–4), 162 (2009).
55. T.A. Bubenik, R.J. Olson, D.R. Stephens, and R.B. Francini. Analyzing the pressure strength of corroded line pipe, in *Proceedings of the International Conference on Offshore Mechanics and Arctic Engineering* (American Society of Mechanical Engineers, 1992), pp. 225–225.
56. F.A.V. Bazána and A.T. Beck, *Corros. Sci.* 74, 50 (2013).
57. P.R. Bergethon, Flow in a chemical potential field: diffusion, in *The Physical Basis of Biochemistry* (Springer, 1998), pp. 445–454.
58. I.A. Blech and C. Herring, *Appl. Phys. Lett.* 29(3), 131 (1976).
59. M. Ganser, F.E. Hildebrand, M. Klinsmann, M. Hanauer, M. Kamlah, and R.M. McMeeking, *J. Electrochem. Soc.* 166(4), H167 (2019).
60. C.O. De González and E.A. García, *Appl. Surf. Sci.* 44(3), 211 (1990).
61. A.J. Bard and L.R. Faulkner, *Electrochemical Methods: Fundamentals and Applications*, vol. 2 (Wiley, New York, 1976).
62. R.H. Nielsen, J.H. Schlewitz, H. Nielsen, and Updated by - Staff. Zirconium and zirconium compounds. *Kirk-Othmer Encyclopedia of Chemical Technology* (2000).
63. D.R. Lide, *CRC Handbook of Chemistry and Physics*, vol. 85 (CRC Press, 2004).
64. S.D. Cramer, B.S. Covino Jr., C. Moosbrugger, B.R. Sanders, G.J. Anton, N. Hrivnak, J. Kinson, C. Polakowski, K. Muldoon, S.D. Henry et al., *ASM Handbook*, vol. 13 (ASM international Materials Park, Ohio, 2003).
65. J.J. Duderstadt and L.J. Hamilton, *Nuclear Reactor Analysis* (Wiley, 1976).
66. X.Y. Zhang, M.H. Shi, C. Li, N.F. Liu, and Y.M. Wei, *Mater. Sci. Eng. A* 448(1–2), 259 (2007).
67. F.A. Gabr, J. Ferrandis, D. Baron, and P. Chantoin, Pressure and composition of gas mixtures in fuel rods for pressurised water reactors by an ultrasonic sensor, in *International Conference on WWER Fuel Performance, Modelling and Experimental Support*, Varna, Bulgaria (2003).
68. R. Kirchheim, *Acta Metallurgica et Materialia* 40(2), 309 (1992).
69. E. Hillner, D.G. Franklin, and J.D. Smee, *J. Nuclear Mater.* 278(2–3), 334 (2000).
70. P.F. Weck, E. Kim, V. Tikare, and J.A. Mitchell, *Dalton Trans.* 44(43), 18769 (2015).
71. J. Chakrabarty and W.J. Drugan, *J. Appl. Mech.* 55, 253 (1988).
72. S. Silvano, Mathematical model of the lame'problem for simplified elastic theory applied to controlled-clearance pressure balances. Preprint [arXiv:1007.0813](https://arxiv.org/abs/1007.0813) (2010).
73. A. Aryanfar, I.I.I.W. Goddard, and J. Marian, *Corros. Sci.* 158, 108058 (2019).
74. X. Chunhua and W. Gao, *Mater. Res. Innov.* 3(4), 231 (2000).
75. D.G. Peters, H.R. Franklin, and R.B. Adamson, in *Sixth International Symposium on Zirconium in the Nuclear Industry* (ASTM STP 824, American Society for Testing and Materials, 1984) p. 507.
76. S.B. Dalggaard, Extended abstracts of the electrochemical society, washington, dc, usa. pp. 82. ASTM STP 824 (1976).
77. F. Garzarolli, W. Jung, H. Schoenfeld, A.M. Garde, G.W. Parry, and P.G. Smerd, Waterside corrosion of zircaloy fuel rods. final report. Technical report, Kraftwerk Union AG (1982).
78. H. Stehle, W. Kaden, and R. Manzel, *Nucl. Eng. Des.* 33(2), 155 (1975).
79. H.C. Berg, Diffusion: microscopic theory, in *Random Walks in Biology* (Princeton University Press, 2018), pp. 5–16.